Title

Delayed dynamic triggering: Local seismicity leading up to three remote M ≥ 6 aftershocks of the 11 April 2012 M8.6 Indian Ocean earthquake

Journal

Journal of Geophysical Research: Solid Earth, 121(1)

ISSN

2169-9313

Authors

Johnson, Christopher W

Bürgmann, Roland

Publication Date

2016

DOI

10.1002/2015jb012243

Peer reviewed

Delayed dynamic triggering: Local seismicity leading up to three remote $M \geq 6$ aftershocks of the 11 April 2012 M8.6 Indian Ocean earthquake

Christopher W. Johnson[1] and Roland Bürgmann[1]

[1] Berkeley Seismological Laboratory and Department of Earth and Planetary Science, University of California, Berkeley, California, USA

Correspondence to: C. W. Johnson, cwj@seismo.berkeley.edu

Abstract

The 11 April 2012 M8.6 strike-slip Indian Ocean earthquake (IOE) was followed by an increase in global seismic activity, with three remote $M \geq 6.0$ earthquakes within 24 h. We investigate delayed dynamic triggering by systematically examining three offshore regions hosting these events for changes in microseismic activity preceding the IOE, and during the hours between the IOE surface-wave arrival and the triggered-event candidate. The Blanco Fault Zone, USA, and the Tiburón Fault Zone, Mexico, each host a strike-slip event, and the Michoacán Subduction Zone, Mexico, hosts a reverse event. At these locations we estimate transient Coulomb stresses of ±1–10 kPa during the IOE. Each study area contains a regional seismic network allowing us to examine continuous waveforms at one or more nearby stations. We implement a short-/long-term-average algorithm and template matching to detect events and assess the seismicity with the β-statistic. Our results indicate low-magnitude seismicity in the days prior to the IOE and the occurrence of earthquakes during the surface-wave passage after more than 2 h of transient loading. We find both transtensional tectonic environments respond to the transient stresses with a substantial increase observed in the seismicity rates during the hours after the passage of surface waves. In contrast, seismicity rates remain constant in the subduction zone we investigate during the 14 h delay between the IOE and the large-magnitude earthquake. The seismicity rate increases we observe occur after many hours of dynamic stresses and suggest the long duration of transient loading initiated failure processes leading up to these $M \geq 6.0$ events.

1 Introduction

Seismic waves from large earthquakes are capable of transferring energy to remote distances, i.e., many fault lengths from the source, which is a well-documented phenomenon and can potentially increase seismic activity in far-field regions [*Freed*, 2005; *Gomberg*, 2001; *Gomberg et al.*, 2004; *Gonzalez-Huizar et al.*, 2012; *Hill and Prejean*, 2015; *Hill et al.*, 1993; *Pollitz et al.*, 2012; *Prejean and Hill*, 2009; *Velasco et al.*, 2008; *West et al.*, 2005]. The 11 April 2012 M8.6 Indian Ocean earthquake (IOE; 08:38:36 UTC; 93.06°, 2.32°, 40 km) is the largest strike-slip earthquake observed in the modern era that ruptured a series of intraplate conjugate faults and was followed by

a M8.2 strike-slip aftershock 2 h after the initial rupture [*McGuire and Beroza*, 2012]. The IOE is interesting with regard to earthquake communication because of the number of large-magnitude ($M \geq 5.5$) events that occurred in the ensuing days. *Pollitz et al.* [2012] quantify the significance of the 6 day increase in remote $M \geq 5.5$ earthquakes following the IOE, and *Johnson et al.* [2015] document the rare occurrence of $M \geq 5.5$ events triggered by global remote $M \geq 7.5$ main shocks, indicating the uniqueness of the large-magnitude remote aftershocks of the IOE. Interestingly, $M > 5$ triggering candidates appear to only occur after a delay period on the order of hours to weeks following the stress perturbation [*Gomberg*, 2013; *Gomberg and Bodin*, 1994; *Gonzalez-Huizar et al.*, 2012; *Parsons et al.*, 2014; *Pollitz et al.*, 2012] and physical evidence to connect these $M > 5$ events to a transient stress via a seismic or aseismic process is lacking. The delay period coupled with a limited number of observations of $M > 5$ triggered events [*Parsons et al.*, 2014] seems to contradict the ubiquity of $M < 5$ triggered earthquakes [*Hill and Prejean*, 2015; *Velasco et al.*, 2008], and the physical process of delayed dynamic triggering still requires a full explanation [*Parsons et al.*, 2012].

Establishing a tenable connection between small transient stresses and a seismic event becomes progressively more difficult as the delay time increases. Nonsystematic delay times of larger-magnitude earthquakes following transient stresses allude to the scenario that multiple failure conditions coincide, e.g., partial damaging of frictional contacts [*Parsons*, 2005] and changes in pore pressure [*Brodsky*, 2003], in order to advance the seismic cycle of $M > 5$ earthquakes to the point of failure. Case studies quantifying seismicity rate changes find that transient stresses on the order of 1–10 kPa are capable of triggering low-magnitude ($M < 4$) earthquakes at remote distances [*Aiken and Peng*, 2014; *Brodsky and Prejean*, 2005; *Pankow et al.*, 2004; *Peng et al.*, 2011b, 2010; *Prejean et al.*, 2004; *Tape et al.*, 2013; *van der Elst and Brodsky*, 2010; *West et al.*, 2005]. Observable changes in seismic activity can be used to infer the state of stress on a fault to further explore earthquake nucleation and help explain the processes initiated during the passage of seismic waves that may be responsible for delayed triggering of subsequent earthquakes [*Brodsky and van der Elst*, 2014; *Harris*, 1998; *Hill and Prejean*, 2015].

The passage of seismic waves can promote two different changes in seismic activity, the first being an immediate increase in earthquakes during the cyclic loading on a fault. This is most easily explained using a Coulomb failure model that assumes the transient stresses exceed a failure threshold on an already critically stressed fault [*Hill*, 2012]. The second is a delayed increase in seismic activity that initiates in the subsequent hours to days of a transient stress [*Freed*, 2005; *Gomberg et al.*, 1998; *Hill and Prejean*, 2015; *Parsons*, 2005]. Proposed models to explain delayed dynamic triggering include nonlinear friction, fluid migration, and/or aseismic deformation [*Hill and Prejean*, 2015]. For a rupture to occur in either dynamic triggering

scenario, a transient load on a preexisting fault late in the seismic cycle is required to advance the fault toward failure [*Gomberg et al.*, 1998, 2004; *Harris*, 1998].

In this study we investigate the delayed dynamic triggering of three $M \geq 6.0$ earthquakes located along the North America Plate boundary within 1 day of the 2012 M8.6 IOE. The global aftershock sequence described by *Pollitz et al.* [2012] contains 16 $M \geq 5.5$ earthquakes in the subsequent 6 days, with three $M \geq 6.7$ main shocks in that set of events. We limit our study to the first 24 h following the IOE and carefully analyze the seismicity leading up to three large earthquakes, which include two $M \geq 6.7$ earthquakes. Our focus is on resolving changes in near-field seismic activity with respect to the transient loading on the faults, specifically in the time period between the passage of seismic waves and these large-event occurrences. The location and orientation of the IOE produced a region of elevated strain along the active plate boundary margins of the Pacific Plate to antipodal distances and encompasses the three events of interest (Figure 1). The rate curve in Figure 1 indicates a multiday increase in global $M \geq 3$ events (see details of analysis described in section 2.3) and motivates the search for a possible increase of low-magnitude events within the vicinity of the three large-magnitude trigger candidates. The three $M \geq 6.0$ trigger candidates are each located offshore in rapidly deforming plate boundary zones, two transform faults and one subduction zone, that regularly host large-magnitude ($M > 5$) earthquakes. The delayed response following the IOE surface waves may indicate that the catalog records are incomplete or an aseismic process is occurring prior to the rupture. For each of the three remote events we systematically investigate changes in microseismic activity preceding the IOE and during the hours between the surface wave arrival and the triggered event candidate using both catalog and waveform data obtained from each region. The methods applied to each region are described in section 2, and the data obtained and the associated results are presented in section 3 for each event of interest.

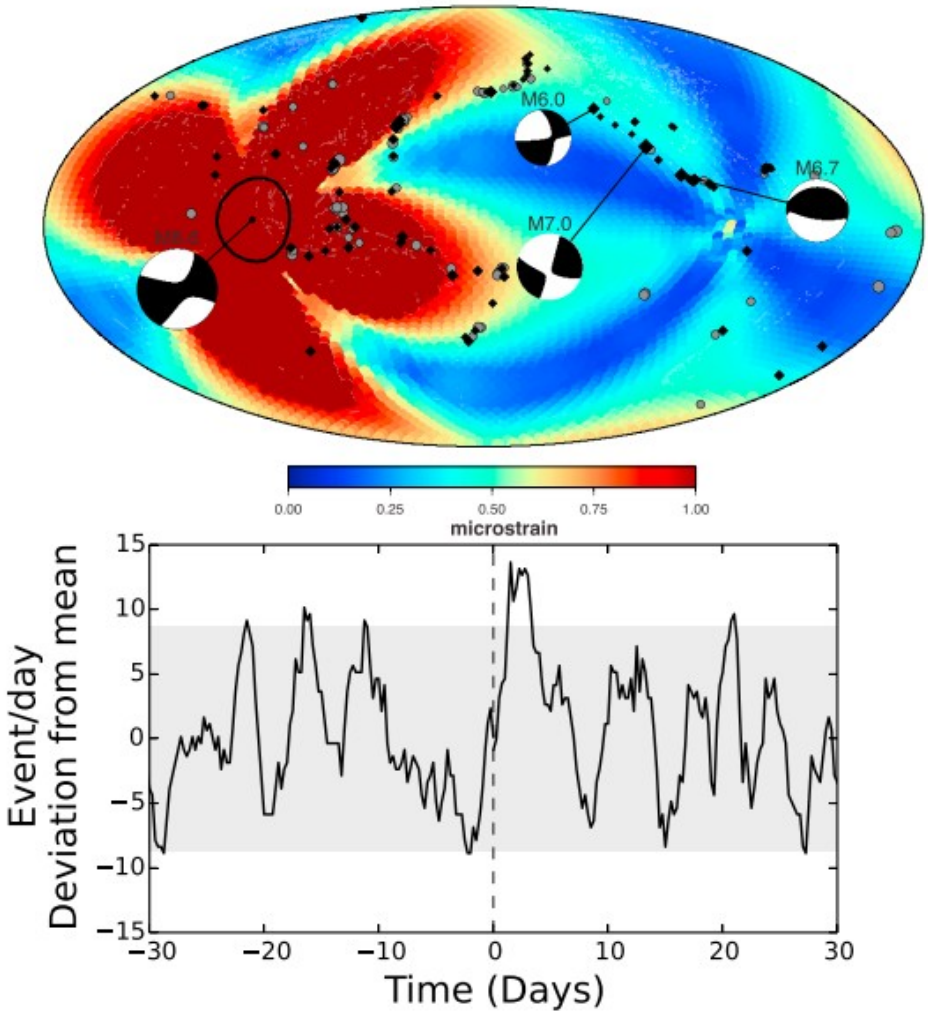

Figure 1. (top) Dynamic strain field for the 11 April 2012 M8.6 IOE calculated from synthetic waveforms. The color represents the peak shear magnitude estimated from the second invariant of the deviatoric strain tensor and, as shown, is saturated at 1.0 μstrain (corresponding to ~30 kPa). Moment tensors (http://earthquake.usgs.gov) are shown for the M8.6 IOE and the three remote $M > 6.0$ main shocks that occurred within 24 h of the transient stress produced by the IOE surface waves. The remote events are located along actively deforming plate boundaries within the elevated strain region. The gray circles and black diamonds show the locations of the $M \geq 3$ declustered seismicity in the 3 days before and after the IOE, respectively. (bottom) The $M \geq 3$ seismicity rate curve from 30 days before to 30 days after the IOE, with two-sigma confidence interval shown in gray for all events located within the elevated strain region (≥0.1 μstrain) with an exclusion zone of 1600 km around the IOE (black circle).

2 Data Analysis Methods

2.1 Seismicity Catalogs

Catalog data were analyzed for the presence of earthquake activity prior to the $M \geq 6$ main shocks. The two sources of catalog events used are the Advanced National Seismic System (ANSS) and the Servicio Sismológico Nacional de Mexico (SSN), which contains lower-magnitude events not reported to ANSS for earthquakes in Mexico. Specifically, we are looking for local activity in the regions of interest preceding the IOE surface waves in order to document ongoing seismic sequences in each study area and any

catalog events during the delay period before the $M \geq 6$ main shocks. We also use all cataloged foreshocks and aftershocks located in the fault zones of interest as templates in the waveform template matching analysis.

2.2 Broadband Waveforms

The waveform data are analyzed for seismic activity during the days to weeks prior to the IOE. The temporal coverage is dependent on network availability in each region and is described in section 3. Due to the offshore location of the three earthquakes of interest and the density of the seismic network coverage, we are limited to a single seismometer for each of the potential triggered main shock locations for the waveform analysis [*van der Elst et al.*, 2013]. The range of distances to the nearest seismometer is between 50 and 100 km, and we use the vertical channel for the analysis.

The waveform data are inspected for evidence of immediate triggering during the passage of the surface waves. We apply a 7 Hz high-pass filter in order to remove teleseismic events and highlight local seismic activity. We calculate the spectrogram for the time series using a ~5 s Hanning window [*Peng et al.*, 2011a] and look for bursts of high-frequency energy superimposed on the long-period signal. In conjunction with the spectral analysis, we generate audio files using the waveform data [*Kilb et al.*, 2012] and listen for earthquakes during the IOE passage and the hours between the local main shock. Following *Kilb et al.* [2012], the audio is combined with the spectral analysis to produce animated time series for 11 April 2012 that are presented in the supporting information. Also included in the supporting information is the spectrogram containing only the time period during the IOE surface wave passage. In addition, we calculate the cumulative energy density [*Brodsky and Prejean*, 2005] during the IOE for multiple bandwidths using

$$E = \rho c \int v^2 dt$$

where ρ is the bulk rock density of 3000 kg m^{-3}, c is the phase velocity of 4500 m s^{-1}, and v is the particle velocity obtained from the waveform data.

To quantify the visual and audio analysis, we perform a single-station event detection analysis using a recursive short-term-average/long-term-average (STA/LTA) algorithm [*Ketner and Power*, 2013; *Withers et al.*, 1998]. The STA/LTA method is widely used in seismological applications and requires tuning of the parameters for regional or global event detection and station noise levels. We start by applying a high-pass filter and use STA/LTA parameters applied to earthquake early warning systems [*Wurman et al.*, 2007], and then adjust for the different noise conditions at each station (Table 1). Our usage of the algorithm is limited to the temporal identification of a local event with no information determined for the location. For this analysis the algorithm was performed on continuous waveform velocity records for the 5 days before the IOE, and we are able to establish a short-term record of activity that is used to calculate a change in seismicity rates following the

IOE. To verify the performance of the algorithm we visually inspect the waveforms of the automated picking process and adjust the parameters based on the inclusion of false event detections. The waveforms for the events selected by the algorithm are presented in the supporting information for each region.

Table 1. IOE Global Aftershocks Within 24 h

Event	Blanco Fracture Zone	Michoacán Sub Zone	Tiburon Fault Zone
M_W	M6.0	M6.7	M7.0
Date	11 April 2012	11 April 2012	12 April 2012
Time (UTC)	22:41:46	22:55:10	07:15:48
Location (°E, °N, depth)	−127.64, 43.58, 8 km	−102.7, 18.23, 20 km	−113.10, 28.7, 13 km
Strike, dip, rake	288°, 81°, 168°	116°, 68°, 95°	311°, 89°, 179°
Distance from IOE	13558 km	17216 km	15644 km
Transient Coulomb stress from IOE	−4.2 – 5.4 kPa	−3.7 – 3.7 kPa	−11.5 – 10.0 kPa
Delay time	14.08 h	14.28 h	22.62 h
STA/LTA Parameters			
Filter Corner	5 Hz high pass	4 Hz high pass	4 Hz high pass
STA/LTA	0.1 s / 5.0 s	0.05 s / 5.0 s	0.05 s / 5.0 s
Trigger on/off	20/12	22/12	22/12

To further look for unreported seismic events we employ a match template technique using longer time periods of waveforms, where available, and use aftershocks from each trigger candidate as templates to identify unreported seismic events [*Kato et al.*, 2013; *Meng and Peng*, 2014; *Peng and Zhao*, 2009; *Shelly et al.*, 2007; *van der Elst et al.*, 2013]. To remove background noise and enhance any local earthquake signal the seismic records are band-pass filtered using a two-pass, four-pole, Butterworth filter with corners of 7–15 Hz. The choice of frequency range is subjective so we test additional frequency ranges of 2–8 Hz and 4–14 Hz and found the higher frequency range produced better results with less false positive detections considering the long distances between the source locations and the seismometer [*van der Elst et al.*, 2013]. Templates are manually selected using the vertical channel of the filtered records by visually searching through the waveform data for earthquakes. All cataloged aftershocks, and the associated secondary aftershocks, are utilized as templates. The template time window is different in the three fault zones due to the travel time required to the nearest seismic station. Regardless of template duration, each starts 1 s before the *P* wave and ends 2 s after the *S* wave arrival. The same filter parameters are applied to the continuous records, and the templates are iterated through the time series to calculate the cross-correlation value at each time step. The median average deviation (MAD) is calculated from the cross-correlation results to determine a positive match threshold. Due to large distances from source to receiver we define a detection threshold of 18 times the MAD of the cross-correlation results to select local seismic activity assumed to be associated with the template. Using a lower multiplier value for the MAD threshold results in an unmanageable number of false positive

detections due to correlation with noise (see supporting information). Other studies have implemented MAD multiplier values between 8 and 15 in order to successfully match microseismicity in the waveforms [*Kato et al.*, 2013; *Meng and Peng*, 2014; *Shelly et al.*, 2007]. Due to the network distance constraints we are able to identify the occurrence of microseismic events with a single station but no information for the magnitude or location is determined when applying this method [*van der Elst et al.*, 2013; *Velasco et al.*, 2008].

2.3 Seismicity Rates

We use the STA/LTA results to calculate a change in seismicity rates using the β-statistic [*Mathews and Reasenberg*, 1988] and is calculated as

$$\beta = \frac{N_a - E(N_a)}{\mathrm{var}(N_a)} = \frac{N_a - N_b \frac{t_a}{t_b}}{\sqrt{N_b \frac{t_a}{t_b}\left(1 - \frac{t_a}{t_b}\right)}},$$

where N_a and N_b are the number of events and t_a and t_b are the time intervals before and after the passage of the IOE surface waves, respectively. The number of events and the time periods are used to calculate the expected number of events and the variance of the number of events afterwards. Following a uniform distribution of events, if no events occur during the time interval t_a, then the expected number of events, $E(N_a)$, is set to 0.25. Usage of the β-statistic requires the assumption that the seismicity is a stationary Poisson process and the value represents the number of standard deviations the rate increases or decreases during the time after. We acknowledge the fact that we are not preconditioning the seismicity data through a declustering procedure to ensure a stationary Poisson process as required for the correct usage of the β-statistic but are limited to the temporal occurrence of events without any information about the magnitude or location. Additionally, we would like to comment on the fact that the choice of starting time will strongly influence the β-statistic calculation and can bias the value if a period of abnormal activity, either high or low, occurs within t_a. Due to data availability limitations, we choose to use a short time period of only 5 days of events selected by the STA/LTA algorithm to test the three regions equally for a seismicity rate change and do not rely solely on the β-statistic values to assess changes in seismic activity. The choice of using the STA/LTA results instead of the template matching results does not change the rate change results.

We also calculate the daily seismicity rate for $M \geq 3$ remote events in the ANSS catalog within ±30 days of the IOE for the spatial region above 0.1 μstrain during the surface wave passage (Figure 1) following *Johnson et al.* [2015]. The rate curve is produced using an ~1600 km exclusion zone around the IOE epicenter to remove local aftershocks. The remote $M \geq 3.0$ events are limited to depths less than 50 km, and the seismicity is declustered using the Reasenberg algorithm [*Reasenberg*, 1985] with default

parameters. The declustering we perform is a first-order approach to remove aftershocks from the rate curve, especially during the days following the IOE when a known global increase in activity occurs. For purposes of this study, a more rigorous declustering effort is not warranted due to catalog completeness differences at the global scale. The rate curve in Figure 1 represents a deviation from the background rate calculated only for the events occurring within the temporal and spatial constraints and is averaged using a 3 day moving window.

2.4 Stress Modeling

The dynamic stresses are calculated in each fault zone using the direct Green's function method to model displacement waveforms and the associated strain [*Friederich and Dalkolmo*, 1995; *Pollitz*, 1996]. The long-period synthetic waveforms are validated using the local seismic records (see supporting information). The stress tensor time series is calculated from the six-component strain tensor time series for an isotropic elastic solid. We assume a Poisson ratio of 0.25 and a shear modulus of 30 GPa, standard values for the seismogenic crust. The stress tensor is rotated to the fault plane, which we assume to have an orientation equal to the strike, dip, and rake of the moment tensor solution and the geometry of the respective plate boundary fault (http://earthquake.usgs.gov). We estimate the transient Coulomb stress using a friction coefficient of 0.4 with the normal and shear components of stress on the fault plane.

3 Study Area, Data, and Results

The three regions of proposed triggered activity shown in Figure 1 are described in chronological order with respect to their time of occurrence following the IOE. Each subsection contains a brief geologic description of the area, the data obtained, and an additional subsection describing the results. Pertinent information for each main shock is summarized in Table 1.

3.1 Blanco Fault Zone, Offshore Oregon, USA

The Blanco Fault Zone (BFZ) is a transform fault system between the Juan de Fuca Plate and the Pacific Plate that links the Juan de Fuca and Gorda spreading ridges located offshore from Oregon, USA (Figure 2). The eastern termination of the BFZ is ~150 km offshore from the Oregon coast and extends ~400 km WNW before intersecting the Juan de Fuca spreading ridge. The fault zone is a series of right-stepping right-lateral transform faults with a long-term slip rate of ~5.6 cm/yr [*Dziak et al.*, 2000; *Wilson*, 1993]. The trigger event candidate in the BFZ we study is the 11 April 2012 (day of year [DOY] 102) M6.0 that ruptured ~14 h after the IOE. Within 56 days prior to the BFZ M6.0, two cataloged events occurred in the fault zone within 10 km of the hypocenter (Figure 2). The first is a M5.8 on 15 February 2012 (DOY046), and a M4.4 occurred on 28 March 2012 (DOY088), possibly an aftershock of the M5.8. The broadband waveform data near the BFZ were recorded by the temporary deployment of ocean bottom seismometers for

the Cascadia Initiative project [*Toomey et al.*, 2014]. We obtained records for the period of 1 February 2012 to 15 April 2012. The distance to the nearest seismic station J06A is ~100 km from the BFZ M6.0 reported location (−127.64°, 43.58°; Figure 2). The next closest station is 170 km from the M6.0. During the IOE surface wave passage we estimate transient Coulomb stress levels from −4.2 to 5.4 kPa (Figure S1). For the analysis, we perform the template matching on waveforms from DOY046–106, and the STA/LTA event picking is performed on the waveforms from DOY097–102.

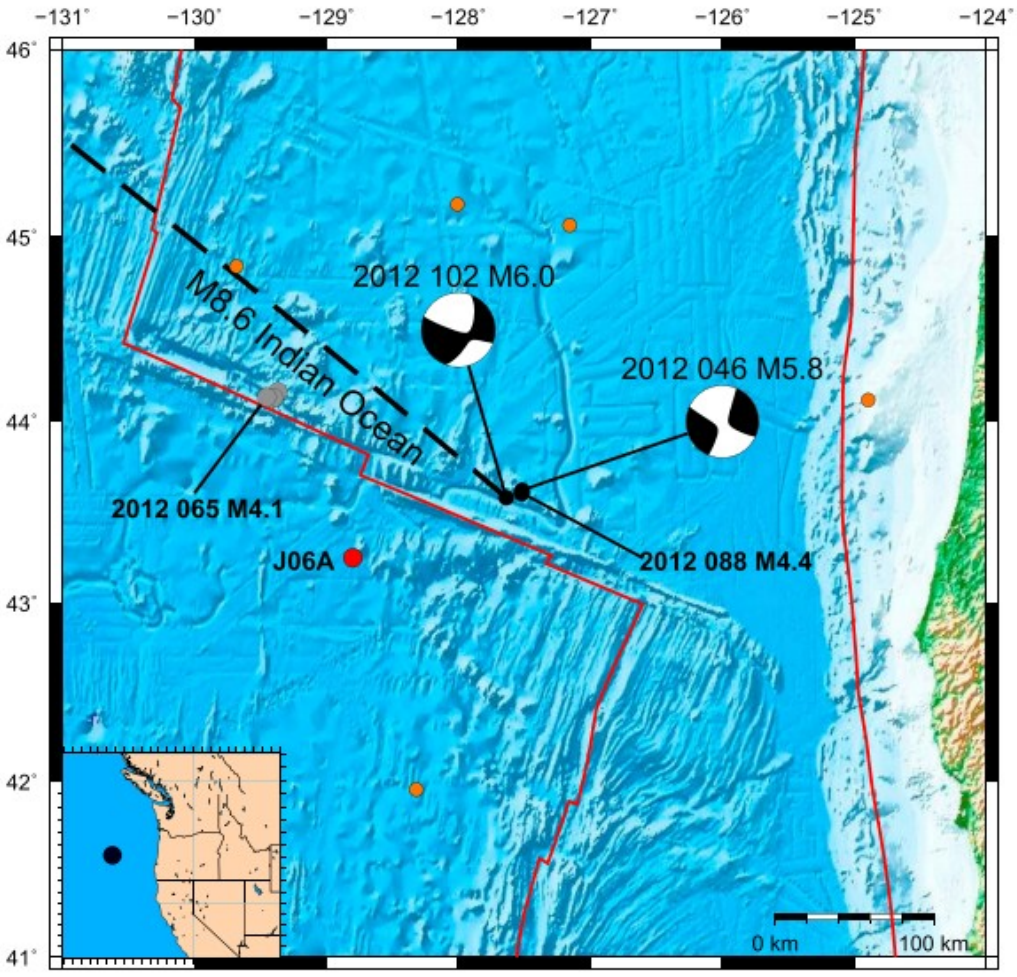

Figure 2. Blanco Fault Zone located offshore Oregon, USA, composed of right-lateral right-stepping transform faults. The dashed black line indicates the back azimuth orientation of the 2012 M8.6 IOE. The red circle is the location of station J06A used in the analysis and is ~100 km from the M6.0. The orange circles are the locations of additional ocean bottom seismometers in the network. Moment tensors (http://earthquake.usgs.gov) are shown for the M5.8 and M6.0 occurring on 02/15/2012 (DOY046) and 04/11/2012 (DOY102), respectively. A M4.4 event occurs 14 days before the M6.0, and three M4.1–M4.3 events occur in the northwest section of the fracture zone 47 days before (DOY065).

3.1.1 Blanco Fault Zone Results

The spectral and audio results suggest local events occurring during the passage of the IOE surface waves, with the first notable event occurring at ~11:15 UTC more than 2 h after the first teleseismic wave arrival (Figures 3

and S4, and Movie S1). The filtered time series and spectrogram shown in Figure 3 indicate three low-magnitude events during the IOE. Movie S1 confirms these events during the IOE surface waves and indicates earthquakes beginning within the first hour of DOY102. The audio in Movie S1 also contains a high-pitch noise that starts after the IOE surface waves, and Figure 3 shows an increase in energy at 15–18 Hz. We further investigate this high-frequency signal by preparing additional audio files and spectrograms, and find it is also present in the daily records from DOY099 to DOY101 at the same frequency range as a discontinuous signal lasting for many hours. We quantify the spectrogram and audio results using the seismicity rates obtained from the STA/LTA algorithm and find an increase in activity beginning on 10 April 2012 (DOY101) that continues to increase during the IOE surface wave passage with the occurrence of 20 events (Figure 4). The cumulative energy density in Figure 5 indicates an increase in high-frequency energy at DOY102.6, which corresponds to the pulse of activity shown in Figure 4 during the delay period. The β-statistic values in Figure 4 are indicative of a positive rate change with values above 2, but we hesitate to state that the subtle change in activity above background levels following the IOE is representative of a rate increase with the very short temporal record used to determine that value.

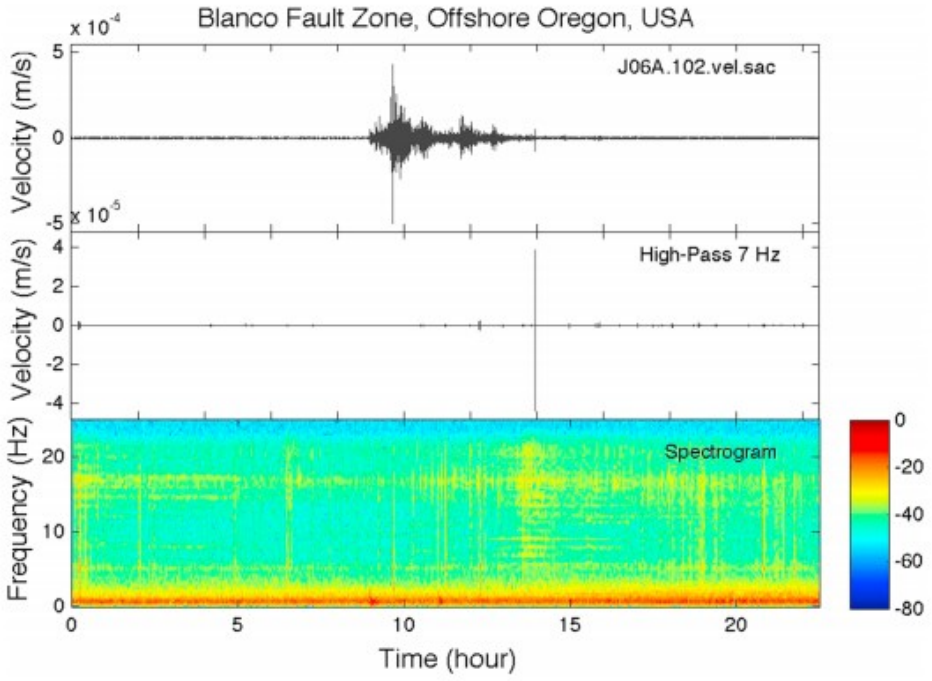

Figure 3. (top) Vertical waveforms of the day of the IOE M8.6 and M8.2 aftershock on 11 April 2012 (DOY102) from 08:20 to 13:50 UTC at station J06A located ~100 km from the BFZ M6.0. The top panel is the original velocity data showing the long-period teleseismic waves. The middle panel is high-pass filtered at 7 Hz to show the near-field earthquakes. The bottom panel is the spectrogram. High-frequency energy shown in the spectrogram indicates near-field events. We find three events that occur ~2 h after the initiation of dynamic shaking (~11.3, ~12.3, and ~13.6) as well as other events occurring throughout the day.

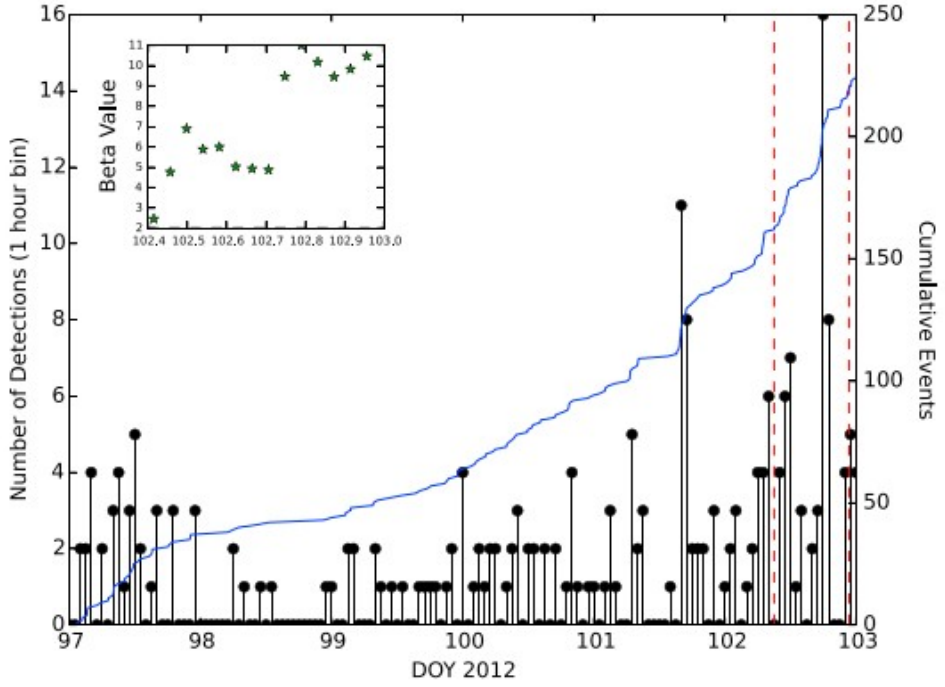

Figure 4. STA/LTA results for the BFZ from 6 to 12 April 2012 (DOY97–103). The blue curve is the cumulative number of events. The black stems are the number of events per 1 h bin. The two dashed red lines represent the time period between the IOE surface waves and BFZ earthquakes. The figure insert is the Beta value calculated for the time period between the dashed red lines. For the β-statistic value the time period before (t_b) is from 97 to the first red dashed line.

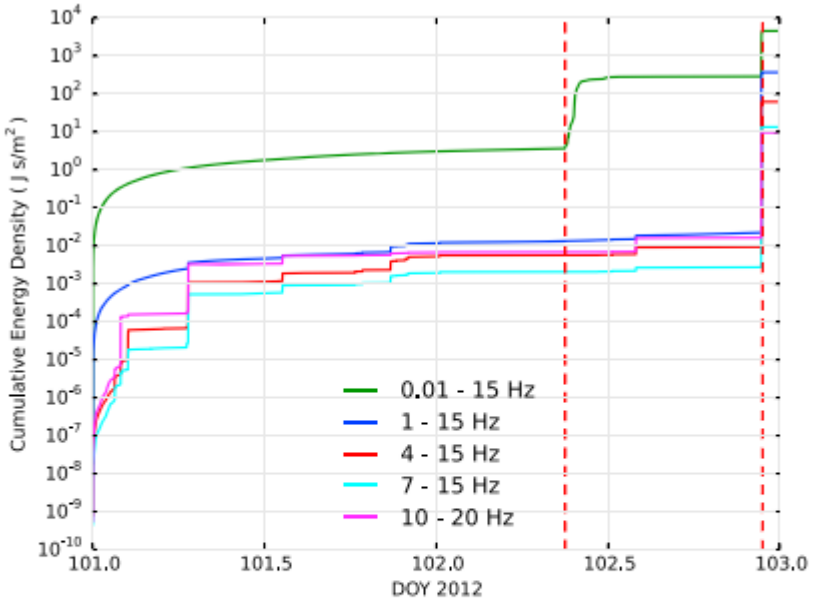

Figure 5. The cumulative energy density is shown for the BFZ using five different bandwidths. Dashed red lines indicate the IOE and local event times. The green line is the greatest and represents the long-period energy from the surface wave arrival. The high-frequency energy increases at DOY102.6 and supports the increase of activity at the same time that is shown in Figure 4.

The ANSS catalog records contain only one aftershock following the M5.8 (DOY046) to use as a known event template. All other templates are selected due to the temporal relation with the known earthquakes in order to limit ourselves to the apparent short-term aftershocks of the cataloged events. Hence, we avoid scanning the entire set of waveforms and selecting every observable event since we lack any location constraint and are working in a seismically active fault zone. We restrict the template selection period to 48 h following the event to reduce the number of nonassociated microseismic events. We manually scan the waveforms following the M5.8, M4.4, and M6.0 and generate 41, 4, and 38 templates from their aftershocks, respectively, using a 13 s duration. The match template correlation coefficient results from the 83 templates are shown in Figure S2. The results are used to produce cumulative and rate curves, which capture the decaying aftershock sequence of the DOY046 M5.8 and DOY102 M6.0 main shocks (Figure 6). The largest increase in the hourly rate of events in Figure 6 does not occur until the BFZ M6.0, but the rate does indicate a similar increase at DOY102.5 that we observe in the STA/LTA results (Figure 4).

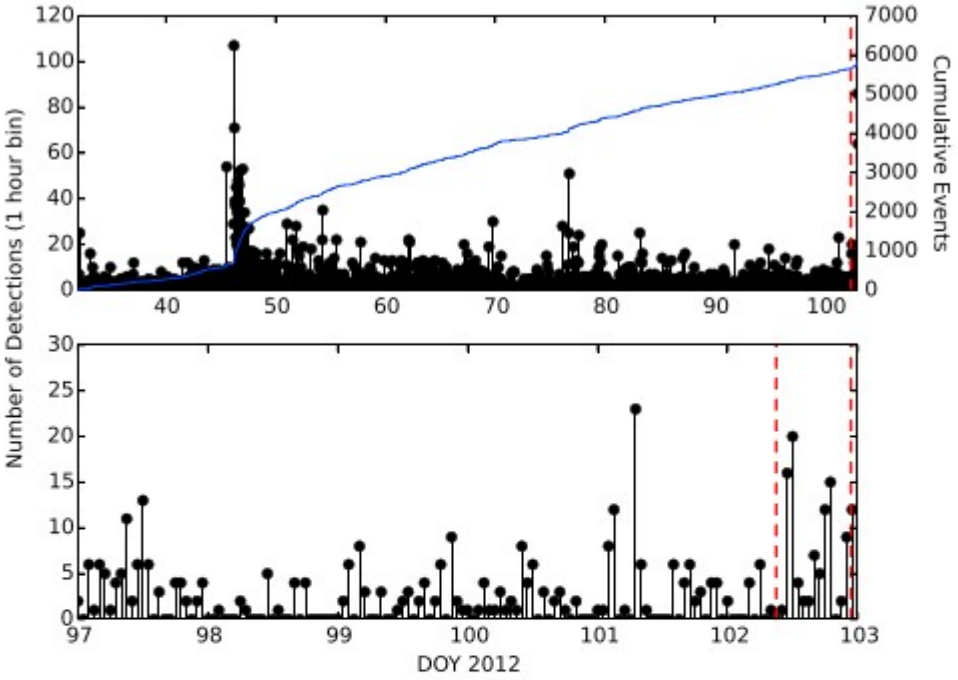

Figure 6. (top) Black stems represent detected events per hour from template matching results using 83 template events from the aftershocks of the 15 February 2012 M5.8 (DOY046), the 28 March 2012 M4.1 (DOY088), and the 11 April 2012 M6.0 (DOY102) main shocks in the BFZ. Overprinted is the cumulative event curve (blue), which indicates the decay of the aftershock sequence following the 15 February 2012 (DOY046) M5.8 earthquake. The bottom panel is a close up of the seismicity rate from 6 to 12 April 2012. The red dashed lines represent the time of the M8.6 IOE and the M6.0 TFZ earthquake. The increase observed during the delay period initiates >2 h after the IOE surface wave arrival.

3.2 Michoacán, Middle America Trench, Mexico

The Michoacán subduction zone segment (MSZ) is located between the subducting Cocos Plate and the North American Plate in southern Mexico. The MSZ is north of Guerrero, Mexico, with a local convergence rate of 5.4 cm/yr [*DeMets et al.*, 2010]. Here the slab is shallowly descending to a depth of 40 km and transitions to a subhorizontal orientation for >100 km before steeply subducting into the mantle [*Pérez-Campos et al.*, 2008]. Near this section of the subduction zone, nonvolcanic tremor and slow slip events are shown to respond to teleseismic surface waves and possibly promote stress redistribution via aseismic creep [*Zigone et al.*, 2012]. The event of interest in the MSZ study area is the 11 April 2012 M6.7 (DOY102) that ruptured ~14 h after the M8.6 IOE surface wave arrival and ~15 min after the M6.0 BFZ event (−102.70°, 18.23°; Figure 7). We obtained seismicity catalog records from the SSN catalog which shows a M4.8 and an associated M3.6 aftershock

are cataloged in the MSZ on 3 April 2012 (DOY094), 8 days before and ~100 km from the M6.7 main shock. Additional seismicity in the MSZ includes a sequence on 8–9 March 2012 of M3.3–M3.8 earthquakes that rupture ~35 km from the main shock and continue propagating ~20 km NW along strike.

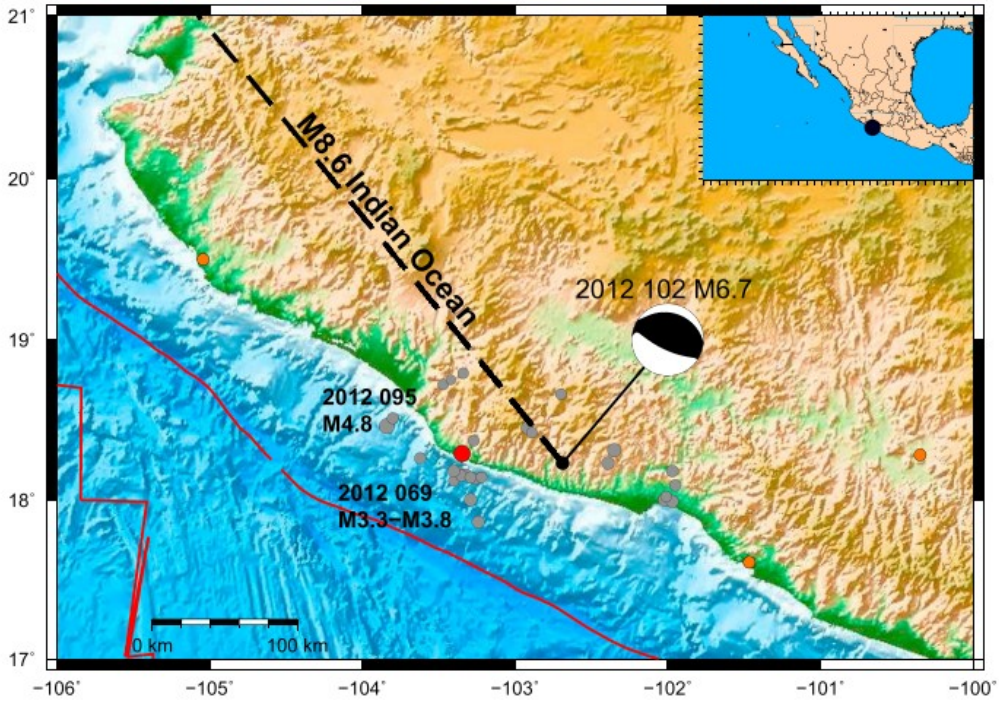

Figure 7. The Michoacán subduction zone earthquake is located in southern Mexico along the Middle America Trench. The 11 April 2012 (DOY102) M6.7 moment tensor (earthquake.usgs.gov) is shown with the black dashed line indicating the back azimuth to the IOE. Red circle is station MMIG, located ~100 km from the M6.7 and used to perform the analysis, and the orange circles are other seismic stations in the region operated by UNAM. Gray circles are the seismicity occurring between 1 March 2012 and 10 April 2012. The locations for the 03 April 2012 (DOY094) M4.8 and the 09 March 2012 (DOY069) M3.8 sequence are labeled. The red lines represent the plate boundary.

The Universidad Nacional Autónoma de México (UNAM) operates a continuously recording seismic network with stations along the coast near the MSZ (Figure 7). We obtained waveform records from 1 to 15 April 2012 for four stations in the vicinity. The station MMIG is the closest to the M6.7 main shock and located at a distance of ~100 from the epicenter. The next closest station is >200 km from the main shock, and both the proximity to the shoreline and distance to the main shock do not create favorable conditions for observing microseismic events. We estimate transient Coulomb stress as high as ±3.7 kPa during the IOE surface wave passage (Figure S2).

3.2.1 Michoacán Results

The high-pass filter, spectrogram, and audio results indicate the occurrence of one event during the surface wave train at hour 11.6 (Figures 8 and S5, and Movie S2). We do observe high-frequency pulses in the high-pass filter data, but upon inspection, these do not appear to be local earthquakes and

are very low-amplitude emergent signals in the data. The spectrogram in Figure 8 does indicate high-frequency energy, but the audio files during this time period do not contain the impulse-like sound that is found for other earthquakes. The STA/LTA produced rate curves (Figure 9) and the cumulative energy (Figure 10) agree that no increase in high-frequency activity is present during the delay period before the MSZ M6.7 event. The β-statistic values for this time period are negative, indicating a reduction in observed events from background levels and can also be seen in the cumulative number of events (Figure 9).

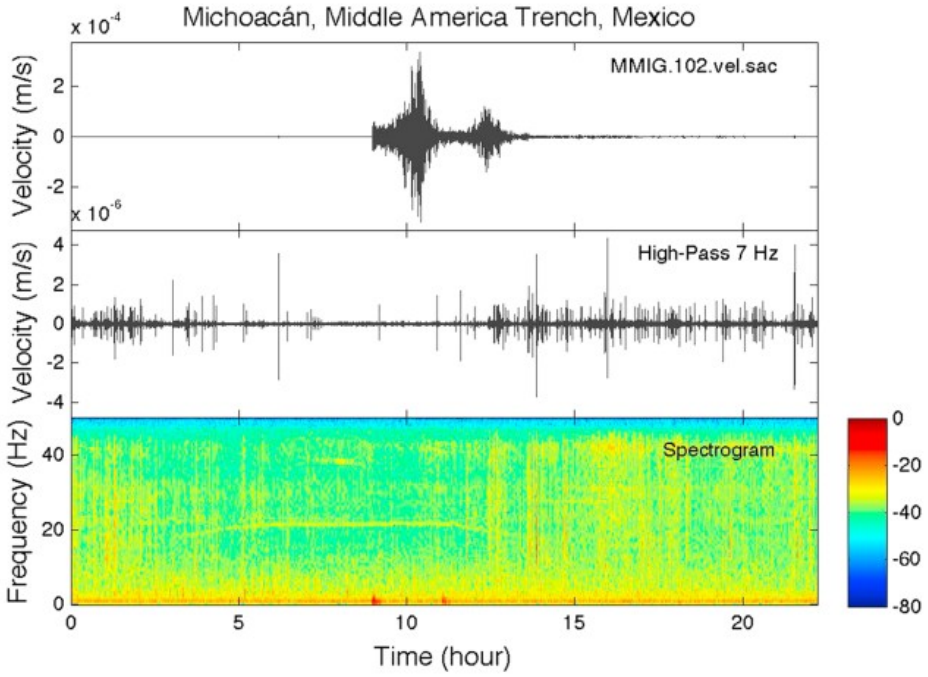

Figure 8. (top) Seismic record for the day of the IOE surface waves for the vertical channel of station MMIG located 100 km from the M6.7 in the MSZ. The top panel is the original velocity data, the middle panel is the high-pass filter data, and the bottom panel is the spectrogram. The high-pass data show high-frequency signals after 12:30 UTC that show an increase in energy in the spectrogram and are consistent with high-frequency energy earlier in the day. Analysis of the audio files (Movie S2) does not suggest that these are local earthquakes, and this signal is observed consistently through the high-pass filter data in the hours and days before the IOE.

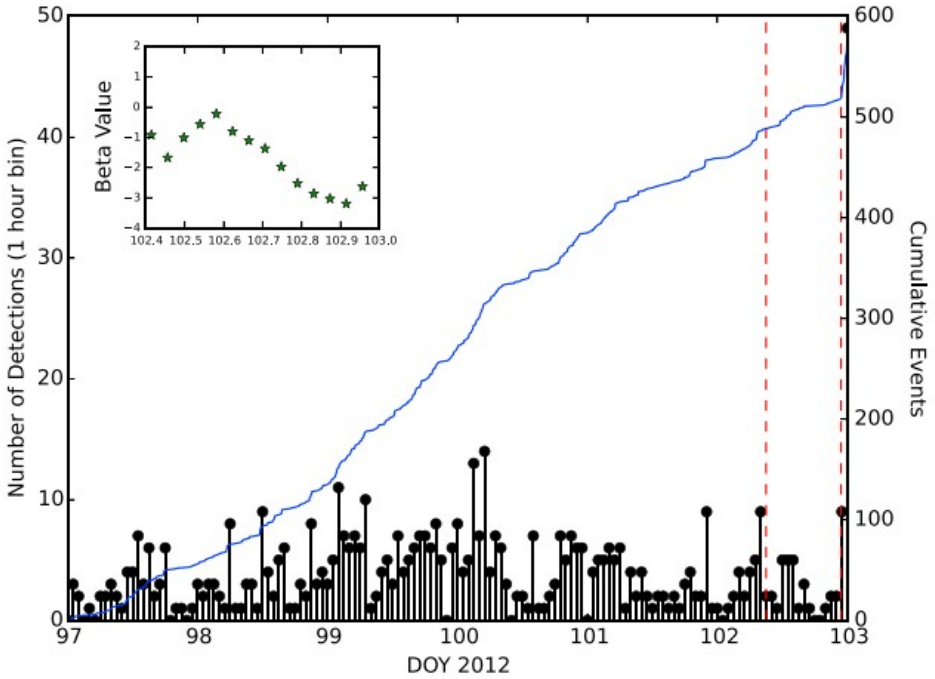

Figure 9. STA/LTA results for station MMIG in the MSZ from 6 to 11 April 2012 (DOY97–103). The blue curve is the cumulative events, and the black stems are events per hour. Dashed red lines indicate the delay period between the IOE surface wave arrival and the MSZ M6.7 earthquake. The figure insert showing the β-statistic values does not indicate an increase during the delay period.

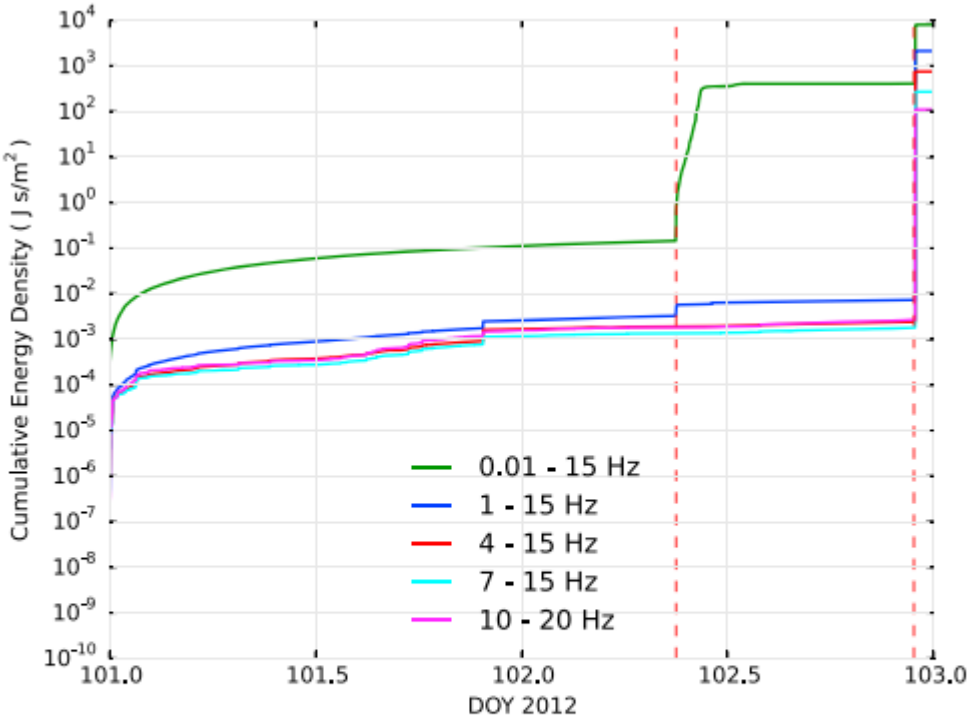

Figure 10. The cumulative energy recorded at station MMIG is shown for multiple bandwidths. The dashed red lines indicate the delay period between the IOE and MSZ earthquakes. No increase in high-frequency energy is observed during the delay period.

Templates are generated using the 19 M6.7 aftershocks within 25 km of the hypocenter listed in the SSN catalog and additional events observed in the MMIG waveforms within 2 days of the main shock. In total, 34 templates with an 11 s duration are used for the analysis. Template results do not indicate a change in seismic activity before the IOE or during the delay period (Figure 11). The results do indicate ongoing microseismic events, but the rates remain constant prior to the M6.7 MSZ main shock.

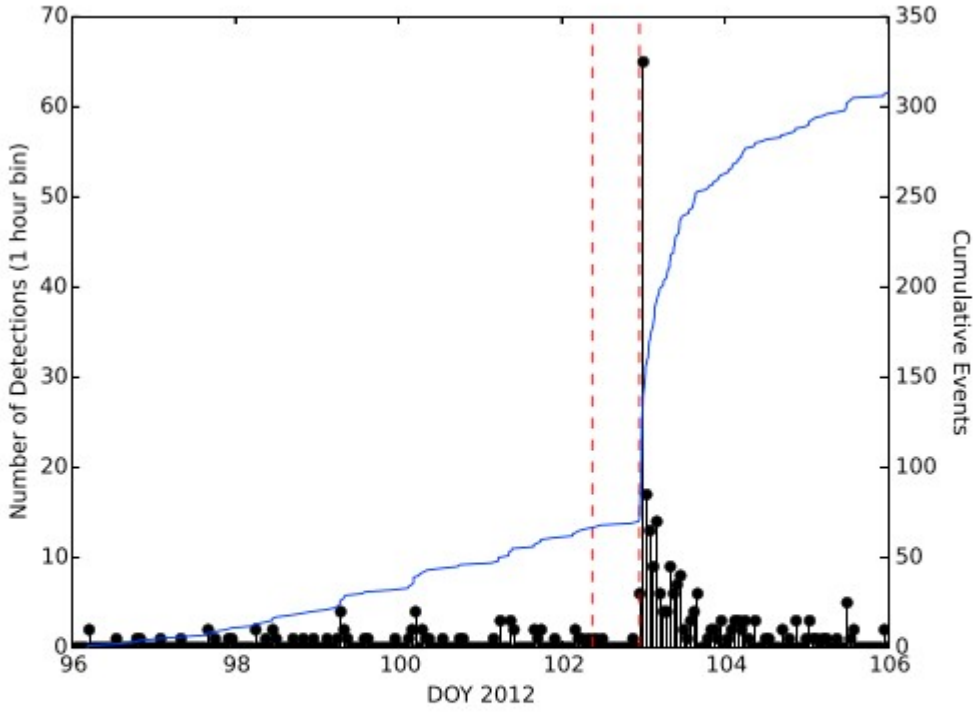

Figure 11. Match template results converted to an hourly rate for station MMIG from 5 to 15 April 2012. Cumulative number of events is shown with blue curve, and the red lines indicate the time of the IOE and MSZ earthquakes. Rate curve does not indicate precursory activity during the delay period between the M8.6 IOE stress perturbation and the M6.7 shown with two red dashed lines.

Interestingly, the arrival time of the M6.0 BFZ seismic waves coincides with the M6.7 MSZ rupture. The ak135 travel time tables [*Kennett et al.*, 1995] indicate the *P* wave and *S* wave arrive 410 s and 90 s before the M6.7, respectively. Visual inspection of the MMIG station records does not clearly show the *P* and *S* wave arrivals due to the signal-to-noise ratio obscuring the expected body waves. Using a distance of 3650 km and velocity of 4.25 km/s, we estimate the Love wave arrival to be ~60 s after the M6.7 MSZ main shock. We model the BFZ waveforms and strain field for the MSZ and calculate a transient stress change between ±0.022 kPa, significantly less than the stresses associated with the IOE, and we do not consider this a likely factor in the failure process.

3.3 Tiburón Fault Zone, Gulf of California, Mexico

Beneath the Gulf of California lies the North America-Pacific Plate boundary that separates mainland Mexico and Baja California, Mexico. The plate boundary is a transtensional shear zone that contains a series of right-stepping right-lateral transform faults and spreading centers. GPS-derived displacement rates indicate ~4.7 cm/yr of lateral motion between North

America and Baja California, Mexico [*Plattner et al.*, 2007]. The Tiburón fault zone (TFZ) is located in the central section of the shear zone and contains en echelon right-lateral transform structures (Figure 12). The event of interest is the 12 April 2012 (DOY103) M7.0 main shock that ruptured ~22 h after the IOE surface waves. The main shock is preceded by four cataloged foreshocks 2 h before, with the largest being a M6.0 that occurred 9 min before the M7.0 main shock. Aside from the foreshocks, seismicity records from the SSN catalog do not indicate an ongoing sequence in the days or months prior to the M7.0 main shock. The SSN catalog shows no earthquakes occurring within 100 km of the main shock for more than 100 days. We estimate a transient Coulomb stress on the TFZ of up to ±10.0 kPa during the IOE surface waves on a fault plane nearly parallel with the back azimuth orientation to the IOE (Figure S3). This favorable fault orientation results in the maximum possible Coulomb stress change during a Love wave passage [*Hill*, 2012], the dominant wave from the IOE.

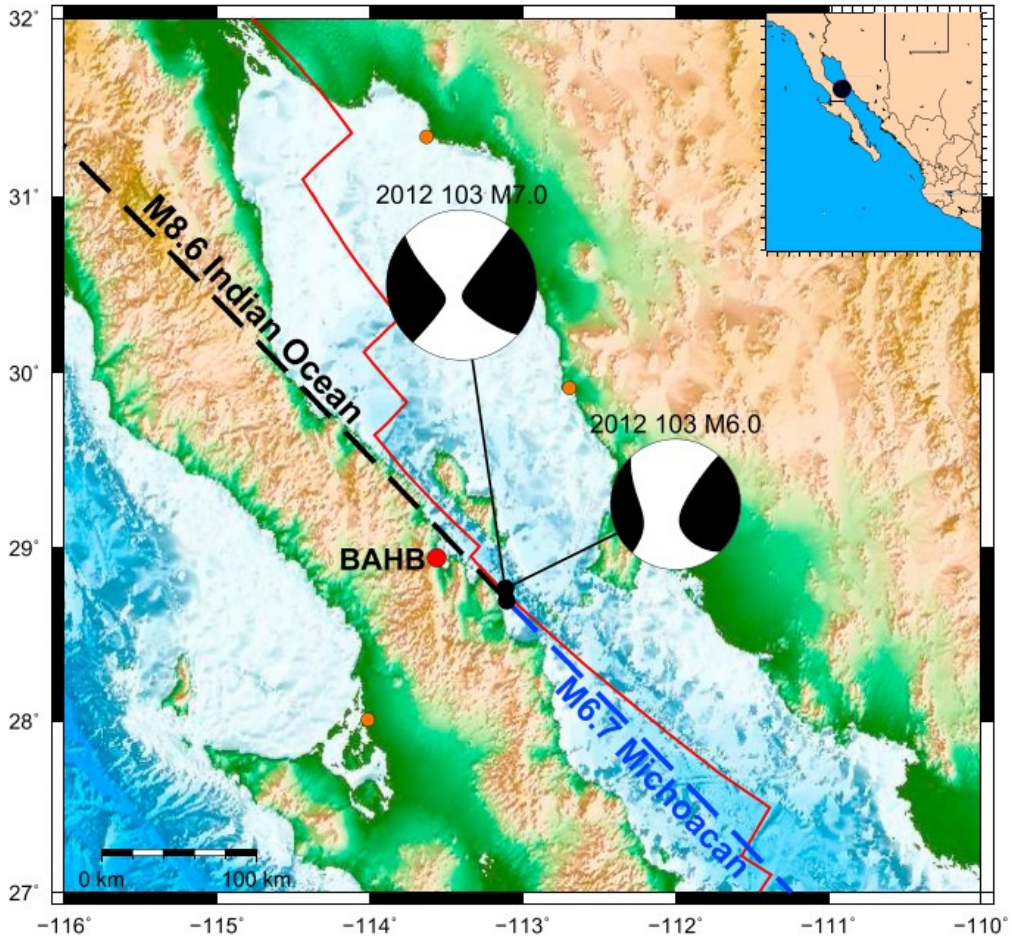

Figure 12. The central Gulf of California TFZ with the 12 April 2012 M6.0 and M7.0 moment tensors (earthquake.usgs.gov). Black and blue dashed lines indicate the back azimuth orientation to the M8.6 IOE and M6.7 MSZ earthquakes. Both travel paths are subparallel to the fracture zone. Station BAHB is shown with a red circle and is located ~50 km from the main shock. Additional stations are shown as an orange circle and are located >125 km from the area of activity with a low signal-to-noise ratio that limits observation of small events.

The TFZ waveform data from 5 to 15 April 2012 were obtained from the Red Seismológica de Banda Ancha del Gulfo de California network operated by Centro de Investigación Cientíca y de Educación Superior de Ensenada (CICESE). The closest station to the TFZ is BAHB, which is located ~50 km from the M7.0 reported location (−113.10°, 28.70°) and recording at 100 Hz (Figure 12). Additional regional seismic stations are located at distances >125 km from the M7.0 main shock and are recording at 20 Hz. The combination of distance and sample rate is not optimal for detecting low-magnitude earthquakes at multiple stations.

3.3.1 Tiburón Fault Zone Results

The TFZ audio results indicate one event during the passage of the M8.2 IOE aftershock surface waves at ~11.5 h as a soft knocking sound following more than 2 h of long-period shaking (Figure S6 and Movie S3). This event is not

clearly identified in the waveforms or the spectrogram (Figure 13) and is presumed to be a low-magnitude local event based on the audio results. We note a high-frequency signal is present in the BAHB data stream, which appears as an emergent signal and persists for many minutes and is shown in the high-pass filter results starting at ~12.25 h (Figure 13). The results in Movie S3 also show the spectrogram for the entire day of 11 April 2012, and the high-frequency energy is present in the early hours of the day and diminishes ~2 h before the IOE wave arrivals, then returns at ~12.25 h. For the purpose of this analysis, we choose to ignore this signal since we cannot match the arrival of the emergent signal at any of the other regional stations. The STA/LTA results (Figure 14) do indicate a seismicity rate increase ~6 h before the TFZ M7.0. This is confirmed with the audio analysis with the rapid succession of foreshocks starting at the beginning of 12 April 2012 (DOY103). Similarly, the cumulative energy also shows an increase in high-frequency energy in the hours prior to the M7.0 (Figure 15).

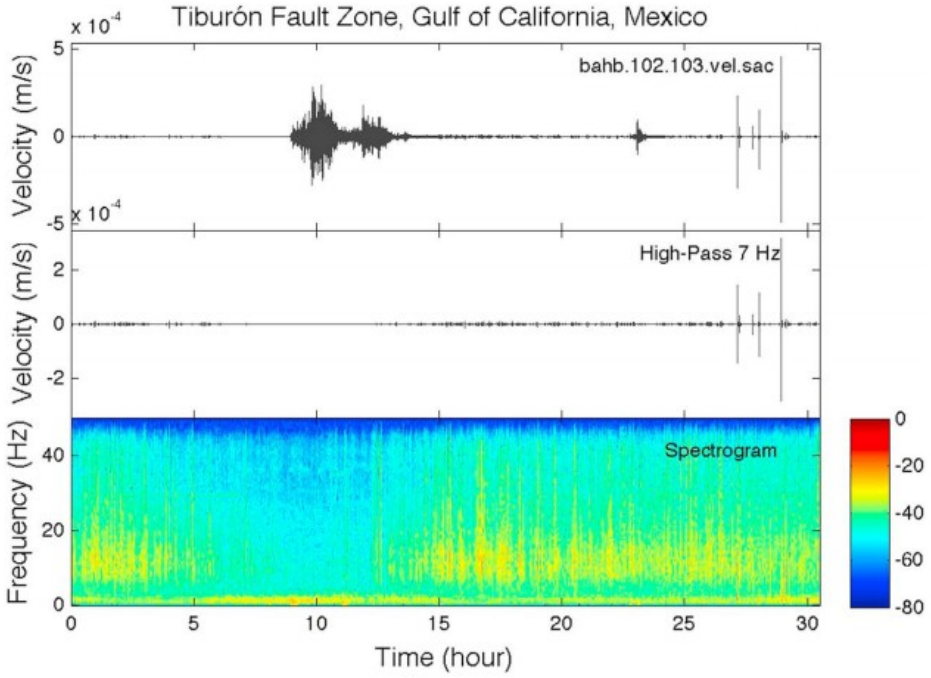

Figure 13. Waveform records of the vertical channel at station BAHB showing the entire day of the IOE and the time period leading up to the TFZ M7.0. The top panel is the original data, the middle panel is the filtered data, and the bottom panel is the spectrogram. The spectrogram does not indicate any evidence for immediate triggering during the IOE surface waves, and this is confirmed with audio files found in Movie S3. The high-frequency energy at ~11.2 h is the arrival of the seismic waves from the M8.2 IOE aftershock. The event at ~23 h is the MSZ M6.7 followed by local foreshocks. We note the presence of minutes-long, tremor-like waveforms with high-frequency energy in both the high-pass filtered waveforms and the spectrogram that are not representative of earthquake activity, and similar signals are present in each day of the waveform records we obtained.

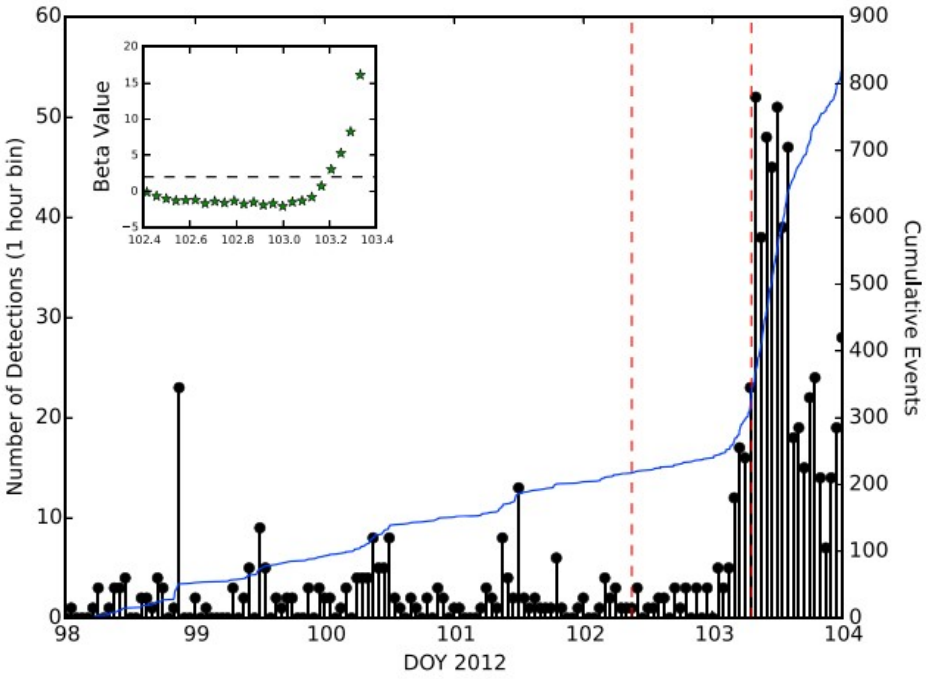

Figure 14. STA/LTA results for station BAHB from 7 to 13 April 2012 (DOY98–104). The blue curve is the cumulative events, and the black stems are the number of detected events per hour. The largest increase in event count occurs in the hours before the TFZ M7.0 (dashed red line on right). The figure insert shows the calculated β-statistic values, which indicate a rate change exceeding 2 standard deviations in the hours before the main shock during the foreshock sequence.

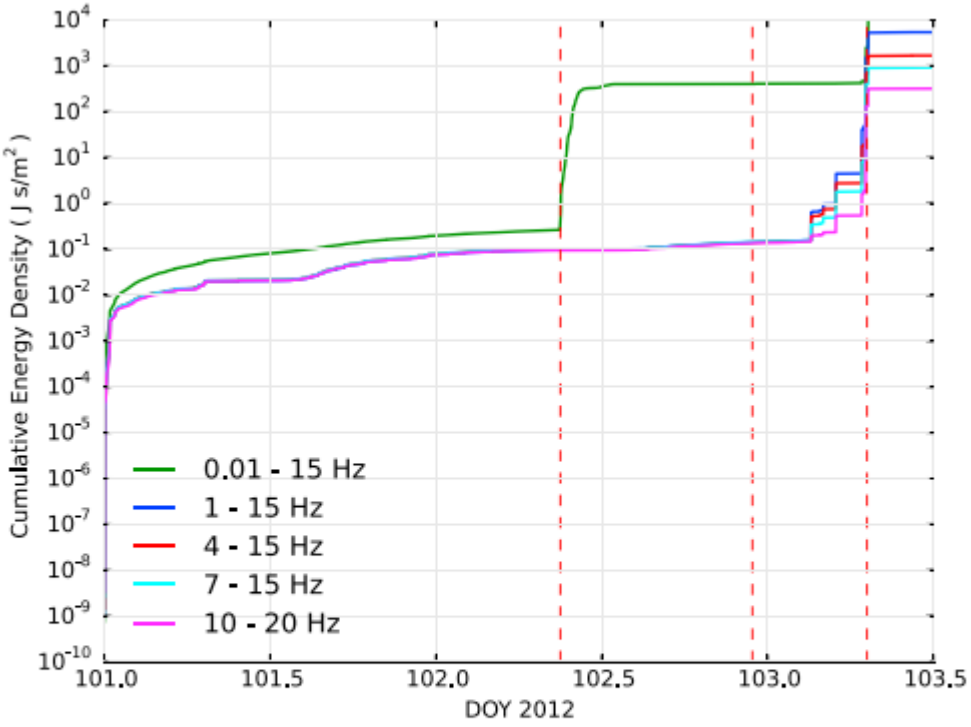

Figure 15. Cumulative energy density is shown for multiple bandwidths. The dashed red lines indicate the times of the IOE, MSZ, and the TFZ from left to right. An increase is observed in the 6 h prior to the main shock and is consistent with the STA/LTA results and the template matching results.

We generate 20 templates with an 8 s duration from the cataloged foreshocks and aftershocks associated with the M7.0 main shock and 73 additional templates from visible inspection of the waveforms for a total of 93 templates. In the template selection process, we carefully select events as impulsive earthquake signals that we detect by manually scanning the waveform records and ignore the emergent signal previously described. The match template results indicate minimal microseismic activity in the 5 days prior to the IOE (Figure 16). Consistent with the spectrogram analysis, we do not find triggered earthquakes during the IOE surface waves or an increase in the first 14 h following the IOE surface waves. We do observe an increase in the seismicity rate in the hour before the surface waves of the M6.7 MSZ main shock, located ~1575 km to the southeast and described in section 3.2, which persists until the M7.0 TFZ main shock and is consistent with the STA/LTA results. We observe a foreshock sequence that initiates following the surface waves from the M6.7 MSZ earthquake, which cascades to the 12 April 2012 04:54 M3.9 SSN catalog event, 145 min before, and the M6.0 foreshock 9 min before the M7.0 TFZ main shock. We estimate the transient Coulomb stress in the TFZ from the M6.7 MSZ at ±0.8 kPa.

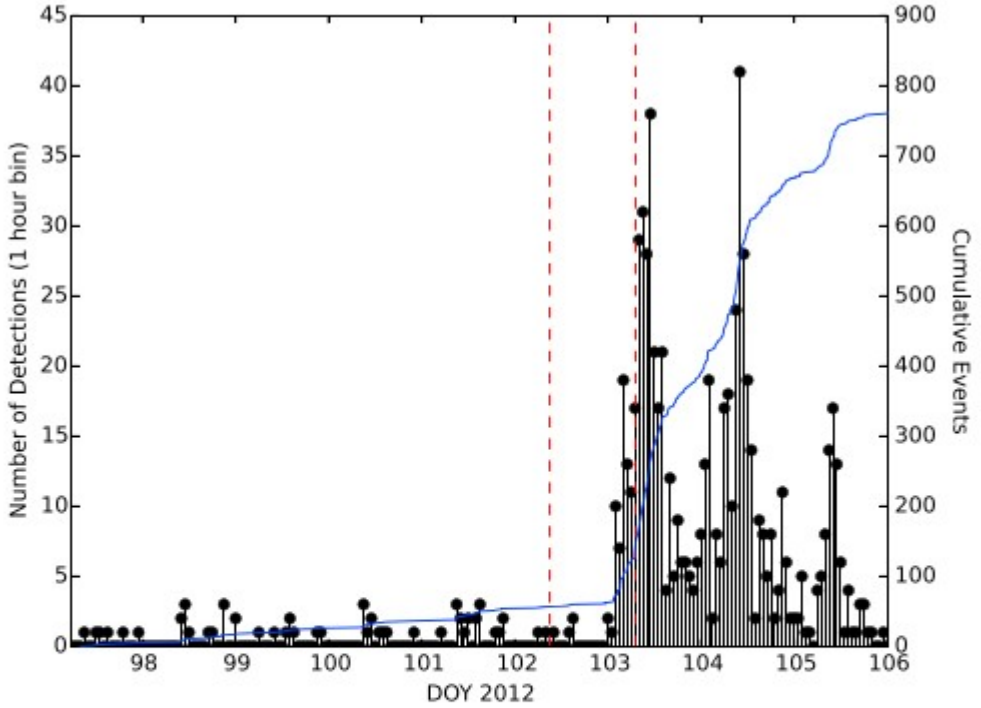

Figure 16. Match template results from the BAHB station are converted to an hourly rate and shown for 6–15 April 2012. The cumulative number of events is shown in blue, and the red lines indicate the time of the M8.6 IOE and M7.0 TFZ earthquakes. Seismicity rate does not increase prior to the M8.6 IOE. The increase in microseismic activity is greatest 15 h after the IOE surface waves and remains elevated until the M7.0 TFZ main shock.

4 Discussion

4.1 Delayed Dynamic Triggering in Each Fault Zone

The three fault zones we investigate each indicate ongoing, low-magnitude seismic activity in both the template matching and STA/LTA results, and this is not surprising for the rapid deformation rates we report in section 3. We do detect a few events during the passage of surface waves, and each of these occurs during the M8.2 IOE aftershock, not during the initial long-period shaking induced by the M8.6 IOE. The spectrogram and audio results indicate three events in the BFZ and one event each in the MSZ and TFZ that were possibly triggered during the M8.2 aftershock. The STA/LTA cumulative event curves show an increase in activity in the BFZ the day before the IOE, the MSZ shows a reduction of events initiating 2 days before, and the TFZ shows a near constant rate of events before the IOE. Essentially, each fault zone contains different changes in seismicity rates during the days before the local main shock, and all three culminate in a $M \geq 6.0$ main shock. To further assess the significance of the rate change we need a much longer time

period of microseismic events that includes location and magnitude to establish a more robust background rate that can support the daily rate fluctuations we observe. With the current data set, this is challenged by the lack of spatial station coverage.

Both the template matching and STA/LTA results for all three study areas do not suggest a change in earthquake rates that initiates with the timing of IOE surface waves. Instead, the change is seismicity rates we observe occurs more than 2 h after the onset of shaking and this delayed response is consistent with catalog studies [*Parsons et al.*, 2014]. *Pollitz et al.* [2012] postulate the long duration (hundreds of seconds) of shaking at elevated strains (>0.1 μstrain or ~3 kPa) is a contributing factor for dynamically triggering large-magnitude events. The immediate triggering we observe supports this argument with fault patches failing during the second period of transient loading. The transient stresses associated with the passage of surface waves from the IOE are variable in each fault zone (Table 1) and are dependent on the source faulting mechanism with respect to the receiver fault orientation and distance from the source [*Gomberg and Bodin*, 1994; *Gonzalez-Huizar and Velasco*, 2011; *Hill*, 2012]. At these remote distances, the transient Coulomb stress changes we estimate from the modeled IOE surface wave displacements are on the order of ±1–10 kPa (Table 1), with the greatest in the TFZ. Our results for the TFZ do provide evidence for a foreshock sequence initiating after multiple episodes of cyclic loading, but we are limited by a high-frequency noise that may mask the onset of additional small events closer in time to the surface waves of the IOE to show a direct seismic connection. A plausible explanation for the delayed response is the transient loading from two remote large-magnitude events with similar location, fault mechanism, and orientation that initiated a failure process, and then the repeat passage of surface waves as they circle the Earth contributed to the large-magnitude triggering [*Peng et al.*, 2011b].

4.2 Triggered $M > 5$ Earthquakes Indicate a Time-Dependent Failure Process

Seismicity catalogs indicate that no $M > 5$ remote earthquakes are known to immediately trigger during the passage of surface waves [*Johnson et al.*, 2015; *Parsons and Velasco*, 2011], with the caveat that global catalog records may be incomplete during the hours following a large-magnitude earthquake [*Iwata*, 2008]. The absence of remote $M > 5$ dynamically triggered earthquakes may suggest that these larger events are not susceptible to immediate failure during the rapidly changing transient stresses during the surface wave passage [*Parsons et al.*, 2012]. Instead, a >8 h delay period after the passage of surface waves appears to be required before the onset of triggered larger events [*Bodin and Gomberg*, 1994; *Gonzalez-Huizar et al.*, 2012; *Parsons et al.*, 2014; *Pollitz et al.*, 2012]. Our results indicating an increase in seismicity rates in the BFZ (Figure 4) and the TFZ (Figure 14) are consistent with a >8 h delay period before a triggered $M > 5$ main shock with the largest perceptible change in microseismicity detected many hours after the onset of transient loading from the IOE earlier

that day. However, we do find events occurring during surface wave passage, suggesting the possibility of a static stress change from these smaller events to critically stressed locked patches that ultimately fail. For this assumption to be plausible, the triggered events must be located very near the main shock hypocenter because static stress changes decay as $1/r^3$ from the source. Using a simple in-plane static shear stress calculation [*Chen et al.*, 2013], a M2 earthquake would result in ~0.66 kPa stress change and a M3 event would result in a ~20 kPa stress change within 1 km of the event. Our data resolution does not allow us to explore the possibility of these static stress changes due to the lack of magnitude and location information of the detected events.

We present evidence showing transient stresses that coincide with $M \geq 6.0$ earthquakes in the following 24 h but do not address the question of whether this global sequence of large-magnitude earthquakes itself could be a random occurrence. Using a compilation of regional earthquake catalogs that include a lower magnitude of completeness for actively monitored regions, *Parsons et al.* [2014] investigate seismicity rate changes following 260 global $M \geq 7.0$ main shocks and do not find a uniform response, with only 2–3% of the main shocks remotely triggering low-magnitude earthquakes. Looking at larger earthquakes spanning a 30 year period, *Parsons and Velasco* [2011] find no increase in $M > 5$ events beyond 1000 km following 205 $M > 7$ main shocks. When examining both catalog and waveform records, the number of observations of $M > 7$ earthquakes remotely triggering earthquakes within the first hour of a stress perturbation deviates below Gutenberg-Richter scaling for the expected number of triggered $M > 5$ earthquakes, given the observed rate of triggered low-magnitude events ($M < 4$) [*Parsons and Velasco*, 2011; *Velasco et al.*, 2008]. This apparent deficit of rapidly triggered $M \geq 5.5$ earthquakes illuminates the challenge of identifying delayed dynamic triggering of larger earthquakes if no evidence exists in the data, either seismic or aseismic, to support the onset of a failure process at the time of a transient stress. Similarly, *Parsons and Geist* [2014] examine clusters of global $M > 5.6$ earthquakes between 2010 and 2014.3 and do not find deviations in the natural fluctuation above the 95% confidence level assuming a temporal Poisson process. However, the IOE is shown to have enhanced $M > 5.5$ for 10 days and suppressed $M > 6.5$ global earthquakes for 95 days, suggesting that transient stresses are altering global fault systems and do require a physical explanation [*Pollitz et al.*, 2012, 2014]. The global increase following the IOE is a unique occurrence that has been observed only once during the 24 h period following a $M \geq 7.5$ main shock when examining 35 years of $M \geq 5.5$ seismicity [*Johnson et al.*, 2015]. Our thorough analysis of seismicity in the three fault zones of interest does produce consistent observations for immediate triggering of a foreshock after >2 h of shaking, but we lack additional data to further investigate the possibility of aseismic deformation occurring between the transient stress and the delayed $M \geq 6.0$ earthquakes.

The 16 $M \geq 5.5$ triggered earthquakes reported by *Pollitz et al.* [2012] all occur more than 14 h after the IOE, suggesting a failure process must exist that is more complex than Coulomb failure for these larger events [*Hill*, 2015]. The IOE did immediately trigger remote tremor and low-magnitude earthquakes ($M < 4$) during the surface wave passage [*Aiken et al.*, 2013, 2015; *Chao and Obara*, 2015; *Fuchs et al.*, 2014; *Gomberg and Prejean*, 2013; *Linville et al.*, 2014; *Tape et al.*, 2013]. However, the data resolution in our study areas is not applicable to resolving triggered tremor. Further exploration of the catalog records for the 12 additional delayed dynamically triggered earthquakes reported by *Pollitz et al.* [2012] indicates that four of these events do have $M < 5.5$ events within 50 km that occur during the time period between the IOE transient stress and the main shock of interest. The first is a M4.4 in offshore Japan on 13 April 2012 in the 2011 M9.0 Tohoku aftershock zone, which occurs temporally between two $M \geq 5.5$ earthquakes rupturing ~30 and ~50 h after the IOE. *Delorey et al.* [2015] attribute the triggering of the two offshore Japan earthquakes to a weakening of the fore-arc normal faults due to dynamic shaking with an observed increase in microseismicity and increase in seismic velocities in the wake of the IOE surface wave train. The second low-magnitude event occurs offshore of Chile on 15 April 2012, 2 days prior to the M6.7 Valparaiso, Chile, main shock. The third event occurs on 19 April 2015, 2 days prior to the M6.7 Papua, Indonesia, main shock. The fourth event occurs on 12 April 2012, 8 days before the M5.7 mid-Atlantic ridge main shock. Consistently, all these earthquakes occur within an active plate boundary zone and do not provide causal evidence for delayed dynamic triggering as the delay times are considerably greater than the 24 h period we more thoroughly investigate. Each of these additional events would require additional analysis that is beyond the scope of this work to verify changes in microseismic activity that can be directly related to the IOE if a seismic station is proximal to the main shock.

Conversely, a M_b5.5 earthquake did rupture in Adak, Aleutian Island, Alaska, 8 min after the M8.6 *P* wave arrival and ~1 min before the *S* wave arrival. Upon visual inspection of the Alaska waveforms, the *S* wave arrival is not clearly observed, but the timing is determined using the ak135 travel time table [*Kennett et al.*, 1995], and this event ruptures several minutes before the large amplitude surface wave arrival. Although not nearly as common as surface-wave triggered earthquakes, *P* waves are capable of triggering tremor [*Ghosh et al.*, 2009; *Shelly et al.*, 2011] and earthquakes near volcanic sources [*Miyazawa*, 2012], and this M_b5.5 may represent another observation of this triggering phenomenon in a volcanic environment.

4.3 Observed Seismicity Changes

Two regions we investigate, the BFZ and TFZ, show an increase in seismic activity many hours after the IOE and before the $M \geq 6.0$ main shocks. In both the BFZ and TFZ, the fault plane orientation is more favorable for maximum Love wave induced transient stress [*Hill*, 2012] with a subparallel

azimuth to the arriving surface waves from the IOE (Figures 2 and 12). Our observations suggest that the triggered main shocks located in transtensional tectonic environments exhibit a more pronounced response to the transient stresses when compared to the compressional environments found in the MSZ. The oblique divergent tectonic environment in these two fault zones is optimal for dynamically triggering $M < 5$ earthquakes due to reduced compressive stress on the faults when compared to convergent tectonic regions [*Hill*, 2015; *Prejean and Hill*, 2009]. The M8.6 IOE could have initiated a time-dependent, but nominally aseismic, failure process during the transient loading [*Shelly et al.*, 2007; *Taira et al.*, 2009]. Then the continued stressing from the surface waves of the M8.2 aftershock provided enough additional loading to immediately trigger the microseismic events we observe (Figures 3 and 13) and further enhance the previously initiated time-dependent failure process that resulted in the delayed dynamic triggering of a $M \geq 6.0$ earthquake.

With regard to the duration of shaking as a contributing factor to delayed dynamic triggering, the TFZ experiences additional transient stressing during the MSZ M6.7 surface wave passage that ruptured 1575 km to the SE as described in section 3.2. Our results indicate a rapid increase in microseismic events following the MSZ main shock that cascade into the M7.0 TFZ earthquake. The seismicity rate curves and the cumulative energy density in the TFZ (Figures 14-16) do indicate an increase before the MSZ M6.7 that continues to increase, and then accelerate, after the additional loading. To note, the calculated transient stress from the M8.2 IOE is 30% (~3.0 kPa) and the MSZ is ~7% (0.8 kPa) of the IOE. However, we suggest that the preferred fault orientation with many hours of cyclic loading in the TFZ prior to the M7.0 primed the fault system for failure and should not be discredited as a contributing factor in the failure process. Considering the fault orientation with regard to peak transient stressing as a contributing factor to the failure process assumes the fault is already late in the seismic cycle. A question that remains is whether the triggered large events would have occurred without the transient loading from the M8.2 aftershock that immediately triggered events in each fault zone. Further studies are needed to differentiate the conditions required to trigger both small and large earthquakes in different tectonic environments, as well as the statistical significance of fluctuations in seismicity with respect to transient loading.

5 Conclusions

We investigate delayed dynamic triggering in three offshore fault zones following the 2012 M8.6 IOE by examining changes in seismicity prior to the rupture of three remote $M \geq 6.0$ main shocks. Template matching and STA/LTA results both suggest ongoing low-magnitude seismicity in each fault zone prior to the IOE. We estimate transient Coulomb stresses on the order of 1–10 kPa for ~4 h during the passage of surface waves from the IOE and an associated M8.2 aftershock. We find possible evidence of immediate triggering of small-magnitude events during the passage of surface waves

from a M8.2 aftershock that occurred 2 h after the IOE. Rate increases occur in two transtensional fault zones prior to the $M \geq 6.0$ main shocks that initiate after multiple hours of transient loading. No change of activity is observed in the subduction environment we investigate, supporting evidence that dynamic triggering is more plausible in extensional environments. We conclude that the long duration of transient loading in conjunction with the occurrence of small earthquakes during the surface wave passage advanced the seismic cycle for the three $M \geq 6.0$ events investigated in this study.

Acknowledgments

We thank the associate editor and two anonymous reviewers for insightful comments that greatly improved the manuscript. We also thank Chastity Aiken, Zhigang Peng, and Fred Pollitz for fruitful discussions that improved an early version of this manuscript. Data products used in this study were accessed through the Northern California Earthquake Data Center (NCEDC), doi:10.7932/NCEDC including the Advanced National Seismic System catalog, which is available at http://quake.geo.berkeley.edu/anss/. Additional catalog data were obtained from the Servico Seismologico Nacional and are available at http://www.ssn.unam.mx/. Moment tensor information was obtained from http://earthquake.usgs.gov. We thank Raul Castro at CICESE for providing waveform data for the TFZ study area. We thank Allen Husker at UNAM for providing waveform data for the MSZ study area. Additional waveform data used in this study are archived at the IRIS Data Management Center (www.iris.edu), including the instruments from the Ocean Bottom Seismograph Instrument Pool (www.obsip.org), which is funded by the National Science Foundation. All figures were produced using GMT4 or Matplotlib. C.W.J. is supported by the National Science Foundation Graduate Research Fellowship under grant DGE1106400. This is Berkeley Seismological Laboratory contribution 2016-2.

References

Aiken, C., and Z. Peng (2014), Dynamic triggering of microearthquakes in three geothermal/volcanic regions of California, *J. Geophys. Res. Solid Earth*, 119, 6992– 7009, doi:10.1002/2014JB011218.

Aiken, C., Z. Peng, and K. Chao (2013), Tremors along the Queen Charlotte Margin triggered by large teleseismic earthquakes, *Geophys. Res. Lett.*, 40, 829– 834, doi:10.1002/grl.50220.

Aiken, C., J. P. Zimmerman, Z. Peng, and J. I. Walter (2015), Triggered seismic events along the eastern Denali fault in northwest Canada following the 2012 Mw 7.8 Haida Gwaii, 2013 Mw 7.5 Craig, and two Mw > 8.5 teleseismic earthquakes, *Bull. Seismol. Soc. Am.*, 105(2B), 1165– 1177.

Bodin, P., and J. Gomberg (1994), Triggered seismicity and deformation between the Landers, California, and Little Skull Mountain, Nevada, earthquakes, *Bull. Seismol. Soc. Am.*, 84(3), 835– 843.

Brodsky, E. E. (2003), A mechanism for sustained groundwater pressure changes induced by distant earthquakes, *J. Geophys. Res.*, 108(B8), 2390, doi:10.1029/2002JB002321.

Brodsky, E. E., and S. G. Prejean (2005), New constraints on mechanisms of remotely triggered seismicity at Long Valley Caldera, *J. Geophys. Res.*, 110, B04302, doi:10.1029/2004JB003211.

Brodsky, E. E., and N. J. van der Elst (2014), The uses of dynamic earthquake triggering, *Annu. Rev. Earth Planet. Sci.*, 42(1), 317– 339.

Chao, K., and K. Obara (2015), Triggered Tectonic Tremor in Various Types of Fault Systems of Japan Following the 2012 Mw 8.6 Sumatra Earthquake, *J. Geophys. Res. Solid Earth*, 120, doi:10.1002/2015JB012566.

Chen, K. H., R. Bürgmann, and R. M. Nadeau (2013), Do earthquakes talk to each other? Triggering and interaction of repeating sequences at Parkfield, *J. Geophys. Res. Solid Earth*, 118, 165– 182, doi:10.1029/2012JB009486.

Delorey, A. A., K. Chao, K. Obara, and P. A. Johnson (2015), Cascading elastic perturbation in Japan due to the 2012 Mw 8.6 Indian Ocean earthquake, *Sci. Adv.*, *1:e1500468*.

DeMets, C., R. G. Gordon, and D. F. Argus (2010), Geologically current plate motions, *Geophys. J. Int.*, 181(1), 1– 80.

Dziak, R. P., C. G. Fox, R. W. Embley, J. L. Nabelek, J. Braunmiller, and R. A. Koski (2000), Recent tectonics of the Blanco Ridge, eastern blanco transform fault zone, *Mar. Geophys. Res.*, 21, 423– 450.

Freed, A. M. (2005), Earthquake triggering by static, dynamic, and postseismic stress transfer, *Annu. Rev. Earth Planet. Sci.*, 33(1), 335– 367.

Friederich, W., and J. Dalkolmo (1995), Complete synthetic seismograms for a spherically symmetric earth by a numerical computation of the Green's function in the frequency domain, *Geophys. J. Int.*, 122, 537– 550.

Fuchs, F., M. Lupi, and S. A. Miller (2014), Remotely triggered nonvolcanic tremor in Sumbawa, Indonesia, *Geophys. Res. Lett.*, 41, 4185– 4193, doi:10.1002/2014GL060312.

Ghosh, A., J. E. Vidale, Z. Peng, K. C. Creager, and H. Houston (2009), Complex nonvolcanic tremor near Parkfield, California, triggered by the great 2004 Sumatra earthquake, *J. Geophys. Res.*, 114, B00A15, doi:10.1029/2008JB006062.

Gomberg, J. (2001), The failure of earthquake failure models, *J. Geophys. Res.*, 106(B8), 16,253– 16,263, doi:10.1029/2000JB000003.

Gomberg, J. (2013), Permanently enhanced dynamic triggering probabilities as evidenced by two $M \geq 7.5$ earthquakes, *Geophys. Res. Lett.*, 40, 4828– 4833, doi:10.1002/grl.50933.

Gomberg, J., and P. Bodin (1994), Triggering of the Ms = 5.4 Little Skull Mountain, Nevada, earthquake with dynamic strains, *Bull. Seismol. Soc. Am.*, 84(3), 844– 853.

Gomberg, J., and S. Prejean (2013), Triggered tremor sweet spots in Alaska, *J. Geophys. Res. Solid Earth*, 118, 6203– 6218, doi:10.1002/2013JB010273.

Gomberg, J., N. M. Beeler, M. L. Blanpied, and P. Bodin (1998), Earthquake triggering by transient and static deformations, *J. Geophys. Res.*, 103(B10), 24,411– 24,426, doi:10.1029/98JB01125.

Gomberg, J., P. Bodin, K. Larson, and H. Dragert (2004), Earthquake nucleation by transient deformations caused by the $M = 7.9$ Denali, Alaska, earthquake, *Nature*, 427(6975), 621– 624.

Gonzalez-Huizar, H., and A. A. Velasco (2011), Dynamic triggering: Stress modeling and a case study, *J. Geophys. Res.*, 116, B02304, doi:10.1029/2009JB007000.

Gonzalez-Huizar, H., A. A. Velasco, Z. Peng, and R. R. Castro (2012), Remote triggered seismicity caused by the 2011, M9.0 Tohoku-Oki, Japan earthquake, *Geophys. Res. Lett.*, 39, L10302, doi:10.1029/2012GL051015.

Harris, R. A. (1998), Introduction to special section: Stress triggers, stress shadows, and implications for seismic hazard, *J. Geophys. Res.*, 103(B10), 24,347– 24,358, doi:10.1029/98JB01576.

Hill, D. P. (2012), Dynamic stresses, Coulomb failure, and remote triggering—Corrected, *Bull. Seismol. Soc. Am.*, 102(6), 2313– 2336.

Hill, D. P. (2015), On the sensitivity of transtensional versus transpressional tectonic regimes to remote dynamic triggering by Coulomb failure, *Bull. Seismol. Soc. Am.*

Hill, D. P., and S. G. Prejean (2015), Dynamic triggering, in *Treatise on Geophysics (2nd Edition)*, edited by G. Schubert, pp. 273– 304, Elsevier, Oxford.

Hill, D. P., et al. (1993), Seismicity remotely triggered by the magnitude 7.3 Landers, California, earthquake, *Science*, 260(5114), 1617– 1623.

Iwata, T. (2008), Low detection capability of global earthquakes after the occurrence of large earthquakes: Investigation of the Harvard CMT catalogue, *Geophys. J. Int.*, 174(3), 849– 856.

Johnson, C. W., R. Burgmann, and F. F. Pollitz (2015), Rare dynamic triggering of remote $M \geq 5.5$ earthquakes from global catalog analysis, *J. Geophys. Res. Solid Earth*, 120, 1748– 1761, doi:10.1002/2014JB011788.

Kato, A., J. I. Fukuda, and K. Obara (2013), Response of seismicity to static and dynamic stress changes induced by the 2011 M9.0 Tohoku-Oki earthquake, *Geophys. Res. Lett.*, 40, 3572– 3578, doi:10.1002/grl.50699.

Kennett, B. L. N., E. R. Engdahl, and R. Buland (1995), Constraints on seismic velocities in the Earth from traveltimes, *Geophys. J. Int.*, 122, 108– 124.

Ketner, D., and J. Power (2013), Characterization of seismic events during the 2009 eruption of Redoubt Volcano, Alaska, *J. Volcanol. Geotherm. Res.*, 259, 45– 62.

Kilb, D., Z. Peng, D. Simpson, A. Michael, M. Fisher, and D. Rohrlick (2012), Listen, watch, learn: SeisSound video products, *Seismol. Res. Lett.*, 83(2), 281– 286.

Linville, L., K. Pankow, D. Kilb, and A. A. Velasco (2014), Exploring remote earthquake triggering potential across EarthScope's Transportable Array through frequency domain array visualization, *J. Geophys. Res. Solid Earth*, 119, 8950– 8963, doi:10.1002/2014JB011529.

Mathews, M. V., and P. A. Reasenberg (1988), Statistical methods for investigating quiescence and other temporal seismicity patterns, *Pure Appl. Geophys.*, 126(2–4), 357– 372.

McGuire, J. J., and G. C. Beroza (2012), A rogue earthquake off Sumatra, *Science*, 336(6085), 1118– 1119.

Meng, X., and Z. Peng (2014), Seismicity rate changes in the Salton Sea Geothermal Field and the San Jacinto Fault Zone after the 2010 Mw 7.2 El Mayor-Cucapah earthquake, *Geophys. J. Int.*, 197(3), 1750– 1762.

Miyazawa, M. (2012), Detection of seismic events triggered by *P*-waves from the 2011 Tohoku-Oki earthquake, *Earth Planets Space*, 64(12), 1223– 1229.

Pankow, K. L., W. J. Arabasz, J. C. Pechmann, and S. J. Nava (2004), Triggered seismicity in Utah from the 3 November 2002 Denali Fault earthquake, *Bull. Seismol. Soc. Am.*, 94(6B), S332– S347.

Parsons, T. (2005), A hypothesis for delayed dynamic earthquake triggering, *Geophys. Res. Lett.*, 32, L04302, doi:10.1029/2004GL021811.

Parsons, T., and E. L. Geist (2014), The 2010–2014.3 global earthquake rate increase, *Geophys. Res. Lett.*, 41, 4479– 4485, doi:10.1002/2014GL060513.

Parsons, T., and A. A. Velasco (2011), Absence of remotely triggered large earthquakes beyond the mainshock region, *Nat. Geosci.*, 4(5), 312– 316.

Parsons, T., J. O. Kaven, A. A. Velasco, and H. Gonzalez-Huizar (2012), Unraveling the apparent magnitude threshold of remote earthquake triggering using full wavefield surface wave simulation, *Geochem. Geophys. Geosyst.*, 13, Q06016, doi:10.1029/2012GC004164.

Parsons, T., M. Segou, and W. Marzocchi (2014), The global aftershock zone, *Tectonophysics*, 618, 1– 34.

Peng, Z., and P. Zhao (2009), Migration of early aftershocks following the 2004 Parkfield earthquake, *Nat. Geosci.*, 2(12), 877– 881.

Peng, Z., D. P. Hill, D. R. Shelly, and C. Aiken (2010), Remotely triggered microearthquakes and tremor in central California following the 2010 Mw8.8 Chile earthquake, *Geophys. Res. Lett.*, 37, L24312, doi:10.1029/2010GL045462.

Peng, Z., L. T. Long, and P. Zhao (2011a), The relevance of high-frequency analysis artifacts to remote triggering, *Seismol. Res. Lett.*, 82(5), 654– 660.

Peng, Z., C. Wu, and C. Aiken (2011b), Delayed triggering of microearthquakes by multiple surface waves circling the Earth, *Geophys. Res. Lett.*, 38, L04306, doi:10.1029/2010GL046373.

Pérez-Campos, X., Y. Kim, A. Husker, P. M. Davis, R. W. Clayton, A. Iglesias, J. F. Pacheco, S. K. Singh, V. C. Manea, and M. Gurnis (2008), Horizontal subduction and truncation of the Cocos Plate beneath central Mexico, *Geophys. Res. Lett.*, 35, L18303, doi:10.1029/2008GL035127.

Plattner, C., R. Malservisi, T. H. Dixon, P. LaFemina, G. F. Sella, J. Fletcher, and F. Suarez-Vidal (2007), New constraints on relative motion between the Pacific Plate and Baja California microplate (Mexico) from GPS measurements, *Geophys. J. Int.*, 170(3), 1373– 1380.

Pollitz, F. F. (1996), Coseismic deformation from earthquake faulting on a spherical earth, *Geophys. J. Int.*, 125, 1– 14.

Pollitz, F. F., R. S. Stein, V. Sevilgen, and R. Burgmann (2012), The 11 April 2012 east Indian Ocean earthquake triggered large aftershocks worldwide, *Nature*, 490(7419), 250– 253.

Pollitz, F. F., R. Burgmann, R. S. Stein, and V. Sevilgen (2014), The profound reach of the 11 April 2012 M 8.6 Indian Ocean earthquake: Short-term global triggering followed by a longer-term global shadow, *Bull. Seismol. Soc. Am.*, 104(2), 972– 984.

Prejean, S. G., and D. P. Hill (2009), Dynamic triggering of earthquakes, in *Encyclopedia of Complexity and Systems Science*, edited by R. Meyers, pp. 2600– 2621, Springer, New York.

Prejean, S. G., D. P. Hill, E. E. Brodsky, S. E. Hough, M. J. S. Johnston, S. D. Malone, A. M. Oppenheimer, A. M. Pitt, and K. B. Richards-Dinger (2004), Remotely triggered seismicity on the United States west coast following the Mw 7.9 Denali Fault earthquake, *Bull. Seismol. Soc. Am.*, 94(6B), S348– S359.

Reasenberg, P. (1985), Second-order moment of central California seismicity, 1969–1982, *J. Geophys. Res.*, 90(B7), 5479– 5495, doi:10.1029/JB090iB07p05479.

Shelly, D. R., G. C. Beroza, and S. Ide (2007), Non-volcanic tremor and low-frequency earthquake swarms, *Nature*, 446(7133), 305– 307.

Shelly, D. R., Z. Peng, D. P. Hill, and C. Aiken (2011), Triggered creep as a possible mechanism for delayed dynamic triggering of tremor and earthquakes, *Nat. Geosci.*, 4(6), 384– 388.

Taira, T., P. G. Silver, F. Niu, and R. M. Nadeau (2009), Remote triggering of fault-strength changes on the San Andreas fault at Parkfield, *Nature*, 461(7264), 636– 639.

Tape, C., M. West, V. Silwal, and N. Ruppert (2013), Earthquake nucleation and triggering on an optimally oriented fault, *Earth Planet. Sci. Lett.*, 363, 231– 241.

Toomey, D., et al. (2014), The Cascadia Initiative: A sea change in seismological studies of subduction zones, *Oceanography*, 27(2), 138– 150.

van der Elst, N. J., and E. E. Brodsky (2010), Connecting near-field and far-field earthquake triggering to dynamic strain, *J. Geophys. Res.*, 115, B07311, doi:10.1029/2009JB006681.

van der Elst, N. J., H. M. Savage, K. M. Keranen, and G. A. Abers (2013), Enhanced remote earthquake triggering at fluid-injection sites in the midwestern United States, *Science*, 341(6142), 164– 167.

Velasco, A. A., S. Hernandez, T. Parsons, and K. Pankow (2008), Global ubiquity of dynamic earthquake triggering, *Nat. Geosci.*, 1(6), 375– 379.

West, M., J. J. Sanchez, and S. R. McNutt (2005), Periodically triggered seismicity at Mount Wrangell, Alaska, after the Sumatra earthquake, *Science*, 308, 1144– 1146.

Wilson, D. S. (1993), Confidence intervals for motion and deformation of the Juan de Fuca Plate, *J. Geophys. Res.*, 98(B9), 16,053– 16,071, doi:10.1029/93JB01227.

Withers, M., R. Aster, C. Young, J. Beiriger, M. Harris, S. Moore, and J. Trujillo (1998), A comparison of select trigger algorithms for automated global seismic phase and event detection, *Bull. Seismol. Soc. Am.*, 88(1), 95– 106.

Wurman, G., R. M. Allen, and P. Lombard (2007), Toward earthquake early warning in northern California, *J. Geophys. Res.*, 112, B08311, doi:10.1029/2006JB004830.

Zigone, D., et al. (2012), Triggering of tremors and slow slip event in Guerrero, Mexico, by the 2010 Mw 8.8 Maule, Chile, earthquake, *J. Geophys. Res.*, 117, B09304, doi:10.1029/2012JB009160.